LETTER • OPEN ACCESS

Active control of localized mode and transmission in topological phononic waveguides by non-Hermitian modulation

OPEN ACCESS
Applied Physics Express **16**, 094001 (2023) LETTER
https://doi.org/10.35848/1882-0786/acf1ef

Active control of localized mode and transmission in topological phononic waveguides by non-Hermitian modulation

Md. Shuzon Ali[1,2], Yusuke Hata[1,2], and Kenji Tsuruta[1,2*]

[1]*Department of Electrical and Electronic Engineering, Okayama University, Japan*
[2]*3-1-1 Tsushima-naka, Kita-ku, Okayama 700-8530, Japan*

[*]E-mail: tsuruta@okayama-u.ac.jp

Received July 11, 2023; revised August 3, 2023; accepted August 17, 2023; published online September 14, 2023

We demonstrate the switching behavioral differences between lossy and nearly lossless edge-mode propagation by non-Hermitian modulation based on the phononic band design of a C_{3v} symmetric, two-dimensional phononic crystal with a unit cell composed of three air-filled circular holes in polydimethylsiloxane. We numerically show that strong loss effects lead to the extinction of the localized modes. This mechanism is analogous to the bound-to-unbound transition in non-Hermitian quantum systems. This result suggests that large variations in non-Hermitian modulation can be used for the active control of edge-mode propagation along topological interfaces. © 2023 The Author(s). Published on behalf of The Japan Society of Applied Physics by IOP Publishing Ltd

Topological phases discovered in quantum systems have triggered extensive explorations of various platforms ranging from photonics to acoustics, and from mechanics to electrics.[1–6] Phononic crystals of a unit cell with C_{3v} symmetry constitute one of the system types that reveals topologically protected robustness as well as topological phase transitions in their dispersion.[7] These systems are commonly assumed to be Hermitian, despite the fact that non-Hermiticity exists in a broad range of systems (known as non-Hermite systems) because of their interactions with the environment that result in gain and/or loss.[8–11] Recent studies have focused on a unique class of non-Hermite systems formed by balanced gain and loss,[12,13] also known as the parity-time (PT) symmetric system.[14] Miri et al.[15] reviewed the recent developments in theoretical and experimental research based on non-Hermiticity, and examined possible extensions from basic science to applied technology. Acoustics can be regarded as a feasible and versatile platform to verify non-Hermitian concepts[16–21] that provide a better understanding and bring non-Hermite physics closer to real applications. The practical realization of both gain and loss in acoustic systems remains a critical issue. Several proposals on the effective non-Hermite Hamiltonian have described coupled acoustic systems with well-designed sound leakages or additional losses.[16,22] Gu et al.[23] explained the basic concepts and mathematical tools required to deal with non-Hermite acoustics by studying pedagogical examples and demonstrated the superior abilities of non-Hermitian modulation for wave manipulation.

However, the loss-only non-Hermite system can be in line with energy dissipation in the real world,[24,25] thus avoiding the introduction of gain[26–28] and simplifying the actual implementation of the non-Hermite topology. Xue et al.[29] reported the experimentally realized passive-symmetric quantum dynamics for single photons by temporally alternating the photon losses in quantum-walk interferometers. Moreover, given that the realization of gain is more challenging to achieve than that of loss, passive non-Hermite systems without gain have been proposed; these systems can exhibit similar physical, extreme asymmetric absorption phenomena.[30,31] Non-Hermitian modulated metamaterials exhibit asymmetric transmission and reflection scattering phenomena.[32–34] Moreover, the transmission of Z-shaped topological waveguides has been shown (experimentally) to be approximately 5% lower than that of a straight waveguide[35,36] Recently, such degradation of robustness in the presence of corners in waveguides has been quantitatively evaluated in terms of the "backscattering length" in valley photonic waveguides.[37–39] However, most of the previous efforts expended to improve transmission efficiency were devoted to the identification of ways to reduce the materials and/or structural losses effectively in waveguides. In this study, we propose the opposite approach. By significantly increasing the losses, we demonstrate that propagation losses, mainly owing to localized modes, can be effectively avoided. We prepared a 2D hexagonal lattice composed of three air-filled circular holes in polydimethylsiloxane (PDMS), wherein localized modes appeared within the phononic band gaps; these modes coupled with the propagating modes (edge modes) that emerged at the interface between neighboring crystalline phases with different band topologies. As the non-Hermiticity parameter (γ) is introduced to modify the phononic band structures, its imaginary parts also emerge, thus leading to possible degradation due to the coupling between the propagating and the lossy localized modes. We analyzed the interface band properties of the supercell and the effects of non-Hermitian modulation. We observed the total output pressure field and transmission along a Z-shaped waveguide constructed by the interface between two oppositely oriented phononic crystals for both Hermite and non-Hermite systems. PDMS is an elastomeric polymer with interesting mechanical properties and excellent optical transparency that can be easily fabricated at very low pressures. In terms of mechanical properties, PDMS can also be regarded as an ideal isotropic and homogeneous material (with a sound velocity closer to that of water and smaller shear stresses than those of solids) that can stably sustain holes filled by gaseous matter. Thus, we used a model system with PDMS, assuming that the longitudinal acoustic modes could be separated distinctly and excited independently from other transverse modes, thus simplifying our examination by focusing only on the pressure acoustics for wave-mechanical analyses. Our present research demonstrates a simple method for designing a topological acoustic waveguide aimed at a switchable wave transmission device based on large variations of the non-Hermiticity parameter (γ). These analyses were based on finite element calculations and simulations using a general-purpose software package (COMSOL Multiphysics).[40]

Initially, we prepared a two-dimensional hexagonal unit cell structure based on valley topological phononic crystals, which were composed of three circular holes (periodically embedded in PDMS and filled with air), as illustrated in Fig. 1(a). We set $a = 2.2$ mm and $d = 0.7$ mm, which define the lattice constant and diameter of each hole, respectively, as proposed by Okuno et al.[41] based on consideration of the ease of fabrication. The speed of sound and the mass density of air were 343 m s^{-1} and 1.293 kg m^{-3}, respectively. In addition, we set the speed of sound and density of PDMS as 1000 m s^{-1} and 1030 kg m^{-3}, respectively. The relative orientation (α) of the rod array in a hexagonal lattice characterizes the symmetry of the structure. At $\alpha = -30°$, the unit cell band structure in the Hermite regime, illustrated in Fig. 1(b), yields two non-trivial dispersive propagating bands (red lines) whose valley Chern indeces[42] at the K point is estimated to be $\pm 1/2$.[43,44] The bandgap, which lies in the frequency range of 438–545 kHz, is between the upper and lower dispersive bands. As α changes to flip the crystal orientation, the band shape is also flipped at $\alpha = 30°$, as depicted in Fig. 1(c), whereas the gap closes when $\alpha = 0°$, as shown in Fig. 1(d). Simultaneously, three flat bands appear at 476.5 kHz, 494.42 kHz, and 505.25 kHz. The modal shapes of these flat bands show the localized nature of the modes near the circular holes, as highlighted in Fig. 1(c) by the black arrows, in contrast to the topologically non-trivial bands indicating non-localized characters of the pressure distributions as highlighted in Fig. 1(c) by the red arrows. These modes are shown to couple with each other when the edge mode generated from the non-trivial modes crosses the flat bands.

In this section, we introduce the non-Hermitian modulation into the system via a loss parameter to observe the mode characteristic as a function of the parameter in the oriented

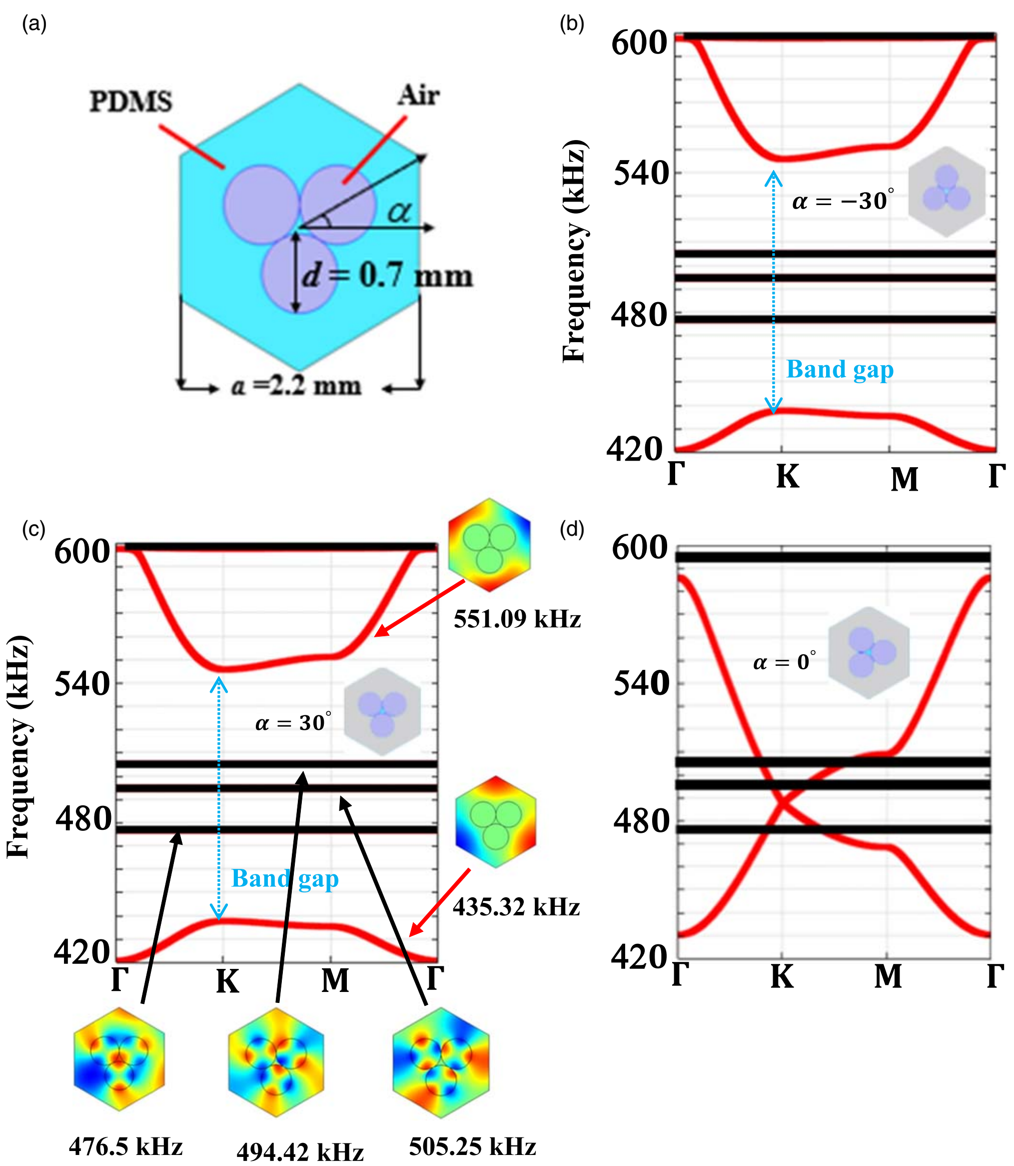

Fig. 1. (a) Hexagonal unit cell at the orientation $\alpha = 30°$. Phononic bandgap for Hermitian system at the orientations (b) $\alpha = -30°$, (c) $\alpha = 30°$, (d) $\alpha = 0°$. The pressure field distributions indicated by the red arrows show propagating dispersive modes at 435.32 kHz and 551.09 kHz, respectively, and those indicated by black arrows depict localized modes at 476.5 kHz, 494.42 kHz, and 505.25 kHz, respectively.

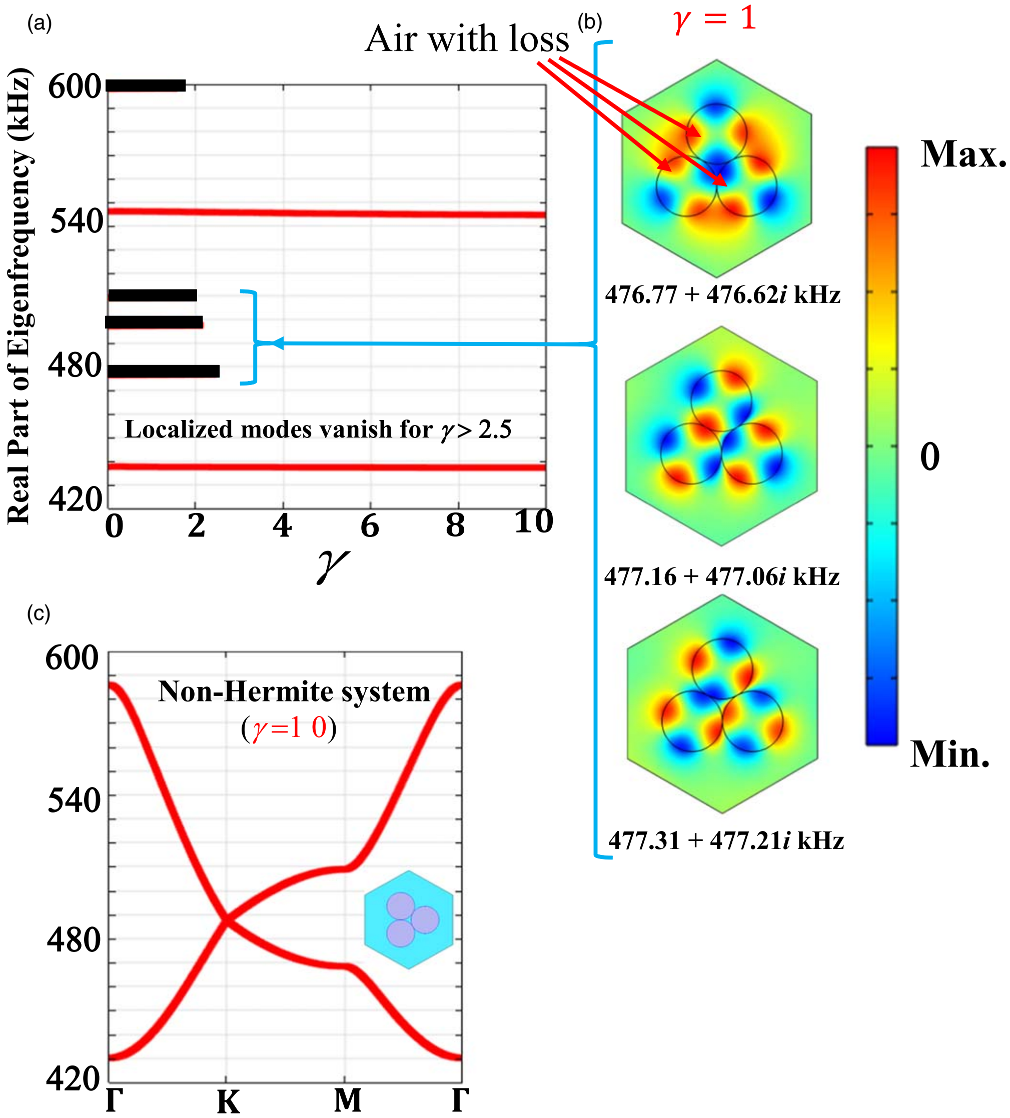

Fig. 2. (a) Variation of the real eigenfrequency as a function of γ. The localized modes are highlighted by the black lines. (b) The pressure field of the three symmetric localized modes (for $\gamma = +1$) with the respective complex eigenfrequencies of $476.77 + 476.62i$ kHz, $477.16 + 477.06i$ kHz, and $477.31 + 477.21i$ kHz, where the color bar highlights the pressure distribution of localized mode in the vicinity of γ. (c) The phononic dispersion of a non-Hermitian lossy system with $\alpha = 0°$.

unit cell ($\alpha = 30°$). To implement the loss effects on fluidic materials filled in the circular hole, we adapted a model in which the speed of sound (c_{air}) was replaced by the complex parameter $c_l = c_{\text{air}}(1 + i\gamma)$. Figure 2(a) shows the real parts of the eigenfrequencies at a point along Γ–K in the Brillouin zone. This reveals that the localized mode (the black lines) appears for the non-Hermite modulation $\gamma < +2.5$. Each of the three degenerate localized modes has a threefold symmetry corresponding to the shape of the unit cell, and the respective complex (lossy) eigenfrequencies are $476.77 + 476.62i$ kHz, $477.16 + 477.06i$ kHz, and $477.31 + 477.21i$ kHz at $\gamma = 1$, as depicted in Fig. 2(b). Conversely, the localized mode (highlighted in black color) vanishes for the non-Hermite modulation when $\gamma > +2.5$, i.e., larger values of the non-Hermiticity parameter in conjunction with its imaginary parts lead to a certain type of extinction of the real eigenvalues. Figure 2(c) shows the band structure of the system with the lossy air in the circular holes of the oriented unit cell ($\alpha = 0°$). Setting the non-Hermitian modulation with $\gamma = 10$, the localized mode disappears and we observe only the valley dispersive modes between the upper and the lower dispersive bands, as depicted in Fig. 1(d). If we apply non-Hermiticity in Figs. 1(b) and 1(c), we also observe only two dispersive bands when $\gamma = 10$. From the examinations described above, we conclude that non-Hermitian modulation can control the switching of localized modes within the bandgap.

Herein, we evaluated the band properties of the valley phononic supercell, where all of the unit cells were composed of circular holes with a C_{3v} symmetry with two orientations ($\alpha = 30°$ and $\alpha = -30°$), as illustrated in Fig. 3(a). The width and height of this supercell structure were a and $\frac{30a}{\sqrt{3}}$, respectively. The interfaces between the upper ($\alpha = 30°$) and lower ($\alpha = -30°$) oriented layers generate topologically protected edge states.[41] Figure 3(b) shows an edge state within the range of 438–490 kHz in the Hermite system ($\gamma = 0$), where two pseudospin modes (highlighted in red) appear at the K+ and K− points (near the K-points in the Brillouin zone of this supercell). Additionally, the localized mode (highlighted in black color) appears between the upper

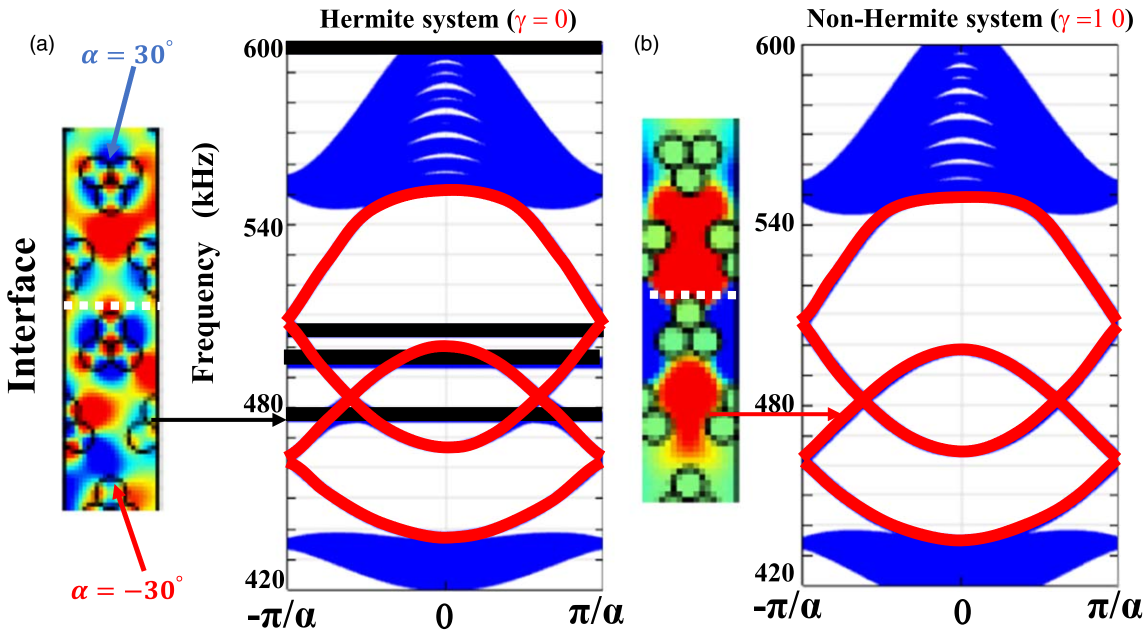

Fig. 3. The pressure field distributions and the valley interface band diagrams of C_{3v} symmetric supercell structure with different orientations ($\alpha = 30°$ and $\alpha = -30°$) of the unit cell layers for (a) Hermitian and (b) non-Hermitian lossy systems, respectively.

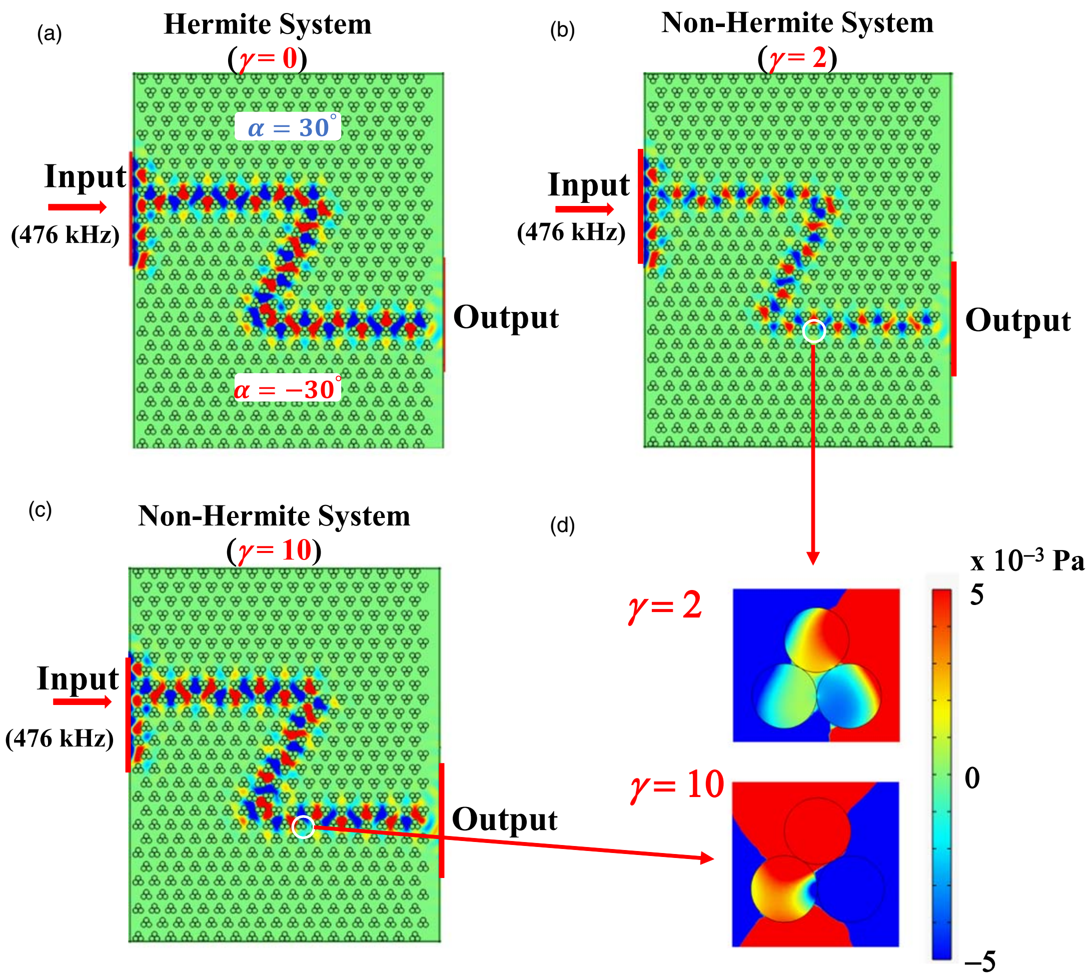

Fig. 4. Normalized total acoustic pressure in a Z-shaped waveguide interface at 476 kHz in (a) Hermitian ($\gamma = 0$) and non-Hermitian lossy systems with (b) $\gamma = 2$ and (c) $\gamma = 10$. (d) Pressure distribution (enlarge) of the Z-shaped waveguide depicted in (b) and (c). [White circles in (b) and (c) highlight the positions of the circular holes depicted in (d)].

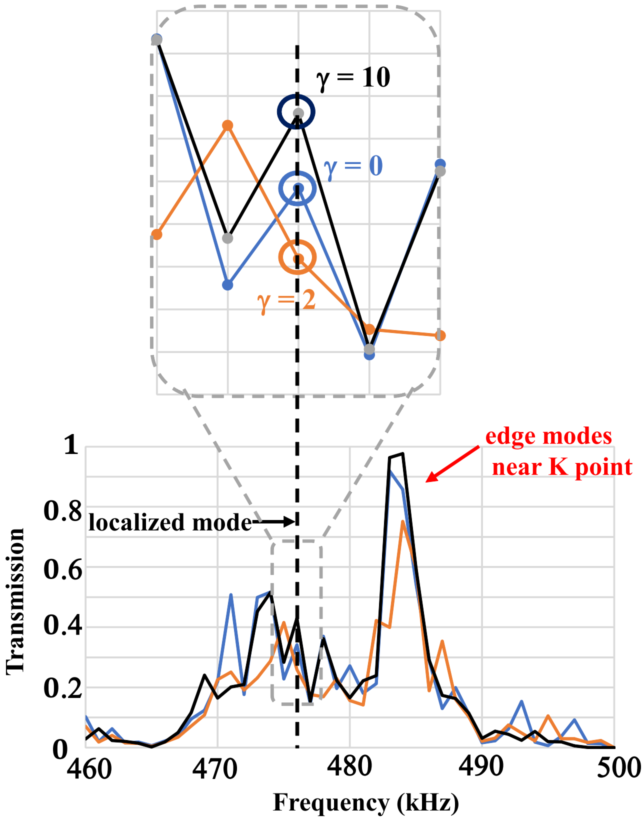

Fig. 5. The transmission spectrum of the Z-shaped waveguide interface in Figs. 4(a)–4(c) (the lower graph) and its magnified view (the upper graph) in the vicinity of the localized mode frequency (476 kHz) indicated by the dashed vertical black line.

and lower bulk modes (highlighted in blue color) in the form of a valley phononic band through the unit cell ($\alpha = 0°$). We then introduce non-Hermiticity such that each circular hole is filled with lossy air. Figure 3(b) also shows that the localized modes are extinct ($\gamma = 10$). In contrast to the ordinary material loss effect, this phenomenon is analogous to the bound-to-unbound transition of quantum states via the non-Hermitian parameter (γ).[45] Because the localized modes are present owing to the resonant effects along the interface between the PDMS and air, the strong loss effect (which suppresses the evanescent waves in the circular holes) inhibits the persistence of the localized modes in cases in which the γ values are greater than a certain value; accordingly, only the eigenfrequency with pure imaginary components can survive.

Based on the above analysis, we performed wave transmission simulations in a Z-shaped waveguide constructed using a topological interface. Topologically protected edge-mode excitation and efficient wave transmission are promising approaches for the observation of acoustic phenomena. The edge-mode excitation and wave propagation in a Z-shaped waveguide interface were examined.[46] Following the application of a 1 Pa incident pressure field in the Hermitian system ($\gamma = 0$), we observed strong edge-mode excitation along the Z-shaped waveguide interface at 476 kHz, as depicted in Fig. 4(a). We then introduced non-Hermiticity such that the circular hole was filled with lossy air. When we set $\gamma = 2$, we observed a weak edge-mode excitation at 476 kHz, as shown in Fig. 4(b). This is because the excited edge mode is coupled with the localized mode excitation that appears at the bulk bandgap frequency for $\gamma = 2$. If we increase the value of the non-Hermitian modulation to a value near 2.5, degradation of the edge-mode propagations can be identified. If we increase the value to $\gamma = 10$, we can observe the recovery of an edge-mode excitation, similar to the case in which $\gamma = 0$, as highlighted in Fig. 4(c), because the localized mode is extinct for a large value of γ. The first figure of Fig. 4(d) clearly shows shorter wavelength modulation of the pressure field inside the holes, implying that the localized mode appears at $\gamma = 2$, whereas the second figure reveals the pressure fields are dominated mostly by the fields outside the holes, indicating the extinction of the localized mode for $\gamma = 10$. The transmission spectrum of the total output pressure along the Z-shaped waveguide interface was calculated as shown in the lower portion of Fig. 5. The small circular shapes with different colors on the dashed vertical black line at the upper portion represent the peak positions at 476 kHz. We observed efficient transmission for $\gamma = 0$ (Hermitian) (as highlighted by the blue circle) at 476 kHz. Although we can observe the lower transmission peak at $\gamma = 2$ (orange circle) owing to the effect of the coupled localized mode, we can also observe a higher transmission peak at $\gamma = 10$ (the black circle). This finding is comparable with the Hermitian system in which $\gamma = 0$. Because the localized mode disappears when $\gamma = 10$, the incident pressure field can excite the edge mode without losing energy due to the coupling with the lossy localized modes.

In conclusion, we found that non-Hermiticity in a 2D acoustic system led to the active control of the localized mode by the extinction of the mode via the non-Hermitian modulation γ. The non-Hermitian modulation yielded a significant effect in non-Hermitian air-lossy systems in which the total acoustic pressure can be transmitted efficiently along the Z-shaped waveguide interface at 476 kHz. Moreover, our results showed that the acoustic wave transmission in a Z-shaped waveguide interface depends on the strong edge-mode excitation and the large non-Hermitian modulation value. The present results can be utilized to fabricate topological, acoustic, and switchable devices in non-energy conserving systems based on valley phononic crystals.

Acknowledgments This research was supported in part by the Japanese Society for the Promotion of Science (JSPS) through KAKENHI Grant Nos. JP21H05020 and JP21K18877.

ORCID iDs Kenji Tsuruta https://orcid.org/0000-0002-1447-2530

1) G. Ma, M. Xiao, and C. T. Chan, Nat. Rev. Phys. **1**, 281 (2019).
2) C. K. Chiu, J. C. Y. Teo, A. P. Schnyder, and S. Ryu, Rev. Mod. Phys. **88**, 035005 (2016).
3) Z. Yang, F. Gao, X. Shi, X. Lin, Z. Gao, Y. Chong, and B. Zhang, Phys. Rev. Lett. **114**, 114301 (2015).
4) X. Zhang, M. Xiao, Y. Cheng, M.-H. Lu, and J. Christensen, Commun. Phys. **1**, 97 (2018).
5) N. P. Armitage, E. J. Mele, and A. Vishwanath, Rev. Mod. Phys. **90**, 015001 (2018).
6) J. K. Asbóth, L. Oroszlány, and A. Pályi, *A Short Course on Topological Insulators* (Springer, Cham, 2016).
7) J.-C. Hsu and T.-T. Wu, Phys. Rev. B **74**, 144303 (2006).
8) H. Schomerus, Opt. Lett. **38**, 1912 (2013).
9) R. El-Ganainy, K. G. Makris, M. Khajavikhan, Z. H. Musslimani, S. Rotter, and D. N. Christodoulides, Nat. Phys. **14**, 11 (2018).
10) Y. Ashida, Z. Gong, and M. Ueda, Adv. Phys. **69**, 249 (2020).
11) Z. Gu, H. Gao, P.-C. Cao, T. Liu, X.-F. Zhu, and J. Zhu, Phys. Rev. Appl. **16**, 057001 (2021).

12) A. Krasnok, N. Nefedkin, and A. Alu, IEEE Antennas Propag. Mag. **63**, 110 (2021).
13) S. Longhi, Europhys. Lett. **120**, 64001 (2018).
14) A. Krasnok and A. Alù, arXiv:2103.08135 (2021).
15) M.-A. Miri and A. Alu, Science **363**, 7709 (2019).
16) W. Tang, X. Jiang, K. Ding, Y. X. Xiao, Z. Q. Zhang, C. T. Chan, and G. Ma, Science **370**, 1077 (2020).
17) V. Achilleos, G. Theocharis, O. Richoux, and V. Pagneux, Phys. Rev. B **95**, 144303 (2017).
18) N. J. R. K. Gerard and Y. Jing, MRS Commun. **10**, 32 (2020).
19) Y. Auregan and V. Pagneux, Phys. Rev. Lett. **118**, 174301 (2017).
20) R. Fleury, D. L. Sounas, and A. Alu, IEEE J. Sel. Top. Quantum Electron. **22**, 121 (2016).
21) S. Puri, J. Ferdous, A. Shakeri, A. Basiri, M. Dubois, and H. Ramezani, Phys. Rev. Appl. **16**, 014012 (2021).
22) D. N. Maksimov, A. F. Sadreev, A. A. Lyapina, and A. S. Pilipchuk, Wave Motion **56**, 52 (2015).
23) Z. Gu, H. Gao, and P.-C. Cao, Phys. Rev. Appl. **16**, 057001 (2021).
24) M. Kawasaki, K. Mochizuki, and H. Obuse, Phys. Rev. B **106**, 035408 (2022).
25) H. Gao, H. R. Xue, Z. M. Gu, T. Liu, J. Zhu, and B. Zhang, Nat. Commun. **12**, 1888 (2021).
26) B. Midya, Annals Phys. **421**, 168280 (2020).
27) S. Xia, D. Kaltsas, D. Song, I. Komis, J. Xu, A. Szameit, H. Buljan, K. G. Markis, and Z. Chen, Science **372**, 72 (2021).
28) H. Zhao, X. Qiao, T. Wu, B. Midiya, S. Longhi, and L. Feng, Science **365**, 1163 (2019).
29) L. Xiao et al., Nat. Phys. **13**, 1117 (2017).
30) D. Li, S. Huang, Y. Cheng, and Y. Li, Sci. China. Phys. Mech. Astron. **64**, 1 (2021).
31) X. Wang, X. Fang, D. Mao, Y. Jing, and Y. Li, Phys. Rev. Lett. **123**, 214302 (2019).
32) R. Fleury, D. L. Sounas, and A. Alu, Phys. Rev. Lett. **113**, 023903 (2014).
33) J. Luo, J. Li, and Y. Lai, Phys. Rev. X **8**, 031035 (2018).
34) M. Lawrence, N. Xu, X. Zhang, Cong, J. Han, W. Zhang, and S. Zhang, Phys. Rev. Lett. **113**, 093901 (2014).
35) M. Kataoka, M. Misawa, and K. Tsuruta, Symmetry **14**, 2133 (2022).
36) K. Tsuruta, Jpn. J. Appl. Phys. **62**, SJ0803 (2023).
37) B. Orazbayev and R. Fleury, Nanophotonics **8**, 1433 (2019).
38) G. Arregui, J. Gomis-Bresco, C. M. Sotomayor-Torres, and P. D. Garcia, Phys. Rev. Lett. **126**, 027403 (2021).
39) M. Patterson and S. Hughes, Phys. Rev. Lett. **102**, 253903 (2009).
40) COMSOL Multiphysics®, v. 6.1. www.comsol.com. COMSOL AB: Stockholm, Sweden (21 September 2022), www.comsol.jp.
41) K. Okuno and K. Tsuruta, Jpn. J. Appl. Phys. **59**, SKKA05 (2020).
42) S. Zheng, G. Duan, and B. Xia, Appl. Sci. **12**, 1987 (2022).
43) T. Fukui, Y. Hatsugai, and H. Suzuki, J. Phys. Soc. Jpn. **74**, 1674 (2005).
44) The numerical estimation of the valley Chern index was performed by integrating the Berry connection with respect to the band along a closed path around the K point See, e.g. ref. 43.
45) V. M. Kulkarni, A. Gupta, and N. S. Vidhyadhiraja, Phys. Rev. B **106**, 075113 (2023).
46) M. S. Ali, M. Kataoka, M. Misawa, and K. Tsuruta, Jpn. J. Appl. Phys. **62**, SJ1002 (2023).